MAKÜFEBED

Mehmet Akif Ersoy Üniversitesi Fen Bilimleri Enstitüsü Dergisi
The Journal of Graduate School of Natural and Applied Sciences of Mehmet Akif Ersoy University
Volume: 16 Issue: 2 - 2025 | Cilt: 16 Sayı 2 - 2025

In Vitro and in Silico Evaluation of Metal Ion Chelated Natural Melanin Nanoparticles for Photothermal Therapy and Magnetic Resonance Performance

Fototermal Tedavi ve Manyetik Rezonans Performansı Üzerine Metal İyonu ile Şelatlanmış Doğal Melanin Nanopartiküllerinin In Vitro ve In Silico Değerlendirilmesi

Melike DEMİRTAŞ[1] Şeyma YEKTAR[2] Gizem KALELİ CAN[3] İbrahim Alpay ÖZCAN[4] Engin BAYSOY[5*] Mustafa Kemal RUHİ[1]

[1] Boğaziçi Üniversitesi, Biyomedikal Mühendisliği Enstitüsü, İstanbul, Türkiye
[2] Üsküdar Üniversitesi, Mühendislik ve Doğa Bilimleri Fakültesi, Yazılım Mühendisliği Bölümü, İstanbul, Türkiye
[3] İzmir Demokrasi Üniversitesi, Mühendislik Fakültesi, Biyomedikal Mühendisliği Bölümü, İzmir, Türkiye
[4] Boğaziçi Üniversitesi, Mühendislik Fakültesi, Elektrik Elektronik Mühendisliği Bölümü, İstanbul, Türkiye
[5] Bahçeşehir Üniversitesi, Mühendislik ve Doğa Bilimleri Fakültesi, Biyomedikal Mühendisliği Bölümü, İstanbul, Türkiye

Article Info

Research Article

DOI: 10.29048/makufebed.1798224

Corresponding Author

Engin BAYSOY

Email: enginbaysoy@gmail.com

Article History

Received: 14.10.2025

Revised: 13.11.2025

Accepted: 17.11.2025

Available Online: 29.12.2025

To Cite

Demirtaş, M., Yekta, Ş., Kaleli Can, G., Özcan, İ. A., Baysoy, E. & Ruhi, M. K. (2025). In vitro and in silico evaluation of metal ion chelated natural melanin nanoparticles on photothermal therapy and magnetic resonance performance. *The Journal of Graduate School of Natural and Applied Sciences of Mehmet Akif Ersoy University, 16*(2), 90-99. https://doi.org/110.29048 /makufebed.1798224

ABSTRACT: Metal ion-chelated natural melanin nanoparticles exhibit strong potential for theranostic applications. However, cross-effects resulting from modifications, whether introduced externally or occurring spontaneously during application, such as the influence of metal ion chelation on photothermal therapy (PTT) efficiency and the effect of PTT-induced temperature changes on MRI contrast, remain poorly understood. This study investigates these interrelated effects through computational modelling and in vitro experiments. Melanin nanoparticles (MNPs) and metal ion-chelated MNPs are synthesized, characterized, and evaluated for cytotoxicity in PC-3 cells. The PTT performance of the less cytotoxic iron-chelated MNPs is compared to that of the unchelated form using COMSOL simulations and in vitro models. MRI contrast is also assessed before and after PTT. Both computational and experimental results show that Fe^{3+}-chelated MNPs exhibit enhanced PTT performance compared to unchelated MNPs, along with a measurable decrease in MRI contrast following treatment. These findings suggest that Fe^{3+}-chelated MNPs are promising theranostic agents capable of delivering effective PTT while enabling MRI-based dosimetric monitoring during cancer therapy.

Keywords: Natural melanin nanoparticles, photothermal therapy, cancer therapies, contrast agents, magnetic resonance imaging

ÖZ: Doğal melanin nanoparçacıklarının (MNP) metal iyonu ile şelatlanmış formları, teranostik uygulamalar için güçlü bir potansiyel sergilemektedir. Bununla birlikte gerek dışarıdan uygulanan modifikasyonların, gerekse uygulama sırasında kendiliğinden ortaya çıkan değişimlerin yol açtığı çapraz etkiler (metal iyon şelatlamasının fototermal terapi (PTT) verimliliği üzerindeki etkisi veya PTT kaynaklı sıcaklık değişimlerinin manyetik rezonans görüntü (MRG) kontrastına etkisi gibi) yeterince anlaşılamamıştır. Bu çalışma, söz konusu karşılıklı etkileri hesaplamalı modelleme ve in vitro deneylerle incelemektedir. Bu çalışmada MNP'ler ve metal iyonu ile şelatlanmış MNP'ler sentezlenmiş, PC-3 hücrelerinde karakterize edilmiş ve sitotoksisiteleri değerlendirilmiştir. Düşük sitotoksisite gösteren demir-şelatlanmış MNP'lerin PTT performansı, şelatlanmamış form ile COMSOL simülasyonları ve in vitro modeller kullanılarak karşılaştırılmıştır. Ayrıca PTT öncesi ve sonrasında MRG kontrastı değerlendirilmiştir. Hesaplamalı ve deneysel bulguların her ikisi de Fe^{3+}-şelatlanmış MNP'lerin şelatlanmamış MNP'lere kıyasla daha yüksek PTT performansı sergilediğini ve tedavi sonrasında MRG kontrastında ölçülebilir bir azalma meydana geldiğini göstermiştir. Bu bulgular, Fe^{3+}-şelatlanmış MNP'lerin etkili bir PTT sağlarken aynı zamanda kanser tedavisi sırasında MRG tabanlı dozimetrik izleme olanağı sunan umut verici teranostik ajanlar olduğunu düşündürmektedir.

Anahtar Kelimeler: Doğal melanin nanoparçacıkları, fototermal terapi, kanser terapileri, kontrast ajanları, manyetik rezonans görüntüleme.

Burdur Mehmet Akif Ersoy University Press
E ISSN: 1309-2243

1. INTRODUCTION

Creating nanoplatforms that are both highly biocompatible and biodegradable while effectively integrating diagnostic and therapeutic (theranostic) capabilities is crucial for the targeted and accurate treatment of diseases. Melanin, a natural biopolymer found in many living organisms, including bacteria, fungi, plants, and animals, is a suitable nanomaterial for photothermal therapy (PTT) of cancer due to its high biocompatibility at the nanoscale and its strong absorption in the visible light spectrum (Solano, 2017; Caldas et al., 2020; Cordero and Casadevall, 2020). Moreover, melanin nanoparticles (MNPs) exhibit strong chelation ability toward metal ions such as Cu^{2+}, Fe^{3+}, and Mn^{2+}, enabling the use of metal ion-chelated MNPs as a positive contrast agent for magnetic resonance imaging (MRI) by shortening T1 relaxation times (Ju et al., 2013; Xu et al., 2017; Chen et al., 2020; Baysoy et al., 2024).

There are theranostic studies in the literature in which melanin and melanin-like nanoparticles have been used simultaneously for both PTT and MRI. For instance, Sun et al. investigated the feasibility of Mn-chelated MNPs as a multifunctional nanoplatform for PTT, combining MRI and photoacoustic dual-modal imaging. According to the results of the study, the nanoparticles presented great laser (808 nm) absorbing capability, negligible cytotoxicity for both in vitro and in vivo experiments, high T1 relaxivity rates, and a good photoacoustic signal (Sun et al., 2018). Similarly, Miao et al. designed PEGylated polydopamine (PDA) nanoparticles chelated with Mn^{2+} to enhance the T1 shortening effect in MRI and achieve photothermal ablation of cancer cells. These nanoparticles generated high contrast under a 9.4 T MRI scanner and exhibited effective PTT on HeLa cells when irradiated with a 2 W, 808 nm laser for 10 minutes (Miao et al., 2015). In another study by Kang et al., Mn^{2+}-doped PDA nanoparticles, which are sensitive to near-infrared light, were designed as multifunctional nanoplatforms for cancer treatment. These nanoparticles demonstrated potential as a combined platform integrating photothermal, photodynamic, and chemotherapeutic effects, providing T1-weighted MR imaging contrast, and were shown to be effective in targeted drug delivery and tumour ablation (Kang et al., 2020). Similarly, Dong et al. synthesized PDA nanoparticles and used them as a platform capable of loading multiple therapeutic and imaging agents. The authors successfully implemented a combination of chemotherapy and PTT with MRI guidance (Dong et al., 2016). These studies collectively highlight the versatility of MNPs for both imaging and therapeutic applications. However, the cross-effects of the manipulations for theranostic applications, such as the effect of metal ion chelation on PTT effectivity, and the impact of PTT-induced temperature increase on MRI contrast have not yet been explored.

This study aimed to investigate the PTT and MRI performance of metal ion-chelated MNPs. Therefore, MNPs and metal ion-chelated MNPs were synthesized, characterized, and evaluated for cytotoxicity in PC-3 cells. The PTT performance of the less cytotoxic iron-chelated MNPs was compared to that of the unchelated form using COMSOL simulations and in vitro models. MRI contrast of iron ion-chelated MNPs was also assessed before and after PTT.

2. MATERIALS AND METHODS

2.1. Synthesis of the MNPs

MNPs were obtained from cuttlefish (Sepia officinalis) ink sacs, following the method reported in the literature (Eom et al., 2017). Ink sacs were immersed in preheated distilled water at 60°C and incubated for 5 minutes. This was followed by the ejection of the dark ink from the sacs using a bistoury, and then the ink was diluted, washed, and centrifuged. The resultant suspension was diluted fivefold, subjected to vortex-mixing, and centrifuged at 10,000 rpm for 20 minutes. After centrifugation, the supernatant was discarded, and the resulting pellet was washed with deionized water. To remove salt and other impurities, the washing and centrifugation process was repeated three times. The collected pellet was then dried in an oven at 80°C for 1-2 days. Dried MNPs were resuspended at a concentration of 1 mg/mL for subsequent experiments and sonicated overnight in a bath sonicator prior to use. During the metal ion chelation process, Mn^{2+} and Fe^{3+} salts were individually mixed with MNP suspensions at final mass ratios of 0.5:1 (Mn:MNP) and 0.1:1 (Fe:MNP), respectively. For each formulation, metal salt solutions (1 mg/mL) were added to 1 mg/mL MNP suspensions in appropriate volumes to achieve the desired ratios, followed by incubation at room temperature for 4 hours. After incubation, the mixtures were centrifuged at 10,000 rpm for 20 minutes, and the supernatants were collected for further analysis.

2.2. Cytotoxicity Experiments

The PC-3 prostate cancer cell line available in our stocks was thawed, maintained, and passaged under routine culture conditions at Boğaziçi University. For toxicity experiments, cells were seeded into 96-well plates at a density of 1×10^4 cells/well and incubated for 24 hours at 37°C in a 5% CO_2 environment. At the end of this period, the cells were incubated for an additional 24 hours with different concentrations of MNP, MNP-Fe^{3+}, and MNP-Mn^{2+}. At the end of the experiment, the cells were analyzed using the MTT assay.

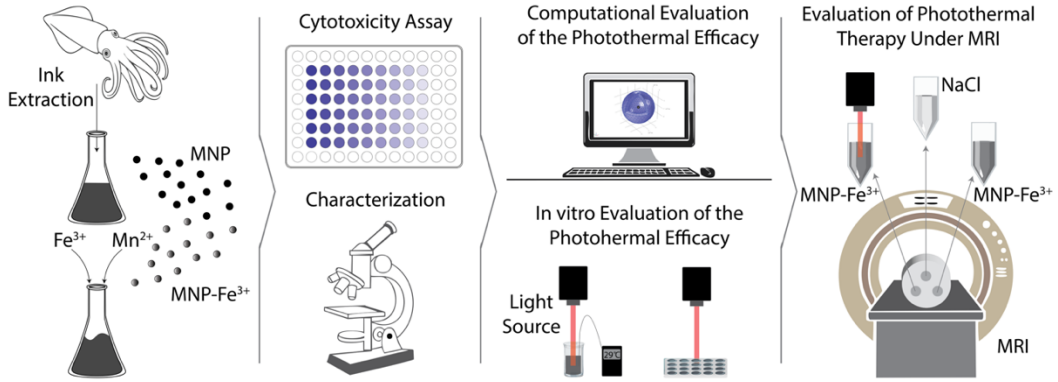

Figure 1. The overview of the study.

2.3. Characterization of the MNPs

The particle size and morphology of MNPs and MNP-Fe^{3+}s were characterized using scanning electron microscopy (SEM) and dynamic light scattering (DLS). SEM provided absolute particle size, while DLS was used to determine the hydrodynamic diameter, polydispersity index (PDI), and zeta potential. Given the tendency of melanin to aggregate, both techniques were employed for reliable characterization. For SEM analysis, nanoparticles were diluted to 0.025 mg/mL, sonicated for 1 hour, drop-cast onto glass slides, air-dried, and sputter-coated with Au–Pd alloy. For DLS, samples were suspended in deionized water (0.025 mg/mL), sonicated for 1 hour, and analyzed at 25°C using quartz cuvettes. Chemical compositions of MNP and MNP-Fe^{3+} were assessed by ATR-FTIR spectroscopy. Finally, the absorbance spectra of the nanoparticles were measured using a NanoDrop 2000c UV–Vis spectrophotometer. Elemental composition analyses were performed using X-ray photoelectron spectroscopy (XPS; Thermo Scientific K-Alpha, UK) to confirm the presence of Fe^{3+} on the nanoparticle surfaces. The chemical structure of MNP-Fe^{3+} was analyzed using ATR–FTIR spectroscopy within the range of 4000–1000 cm^{-1}.

2.4. Simulation of the Nanoparticles and Light Irradiation

The effects of nanoparticle size and iron chelation on light absorption, as well as resulting heating capacity, are difficult to investigate experimentally. First, controlling the size of the synthesized nanoparticles is challenging. Second, absorbance values are highly dependent on concentration; thus, any variation in the amount of MNP or MNP-Fe^{3+} during weighing can alter the results and introduce errors. To develop a reliable method, model validation was conducted through simulations using the finite element method in COMSOL Multiphysics. This process involved constructing geometry, defining the relevant physics and boundary conditions, generating the mesh, performing the simulation, and evaluating the outcomes. First, the specific physical and chemical characteristics of MNP, such as size, shape, material density, specific heat capacity, and properties of the environment (distilled water), as well as thermal conductivity, were defined. The characteristics of the laser source and the distance between the laser source and the optical absorption and diffusion variables were selected consistently with real experiments. After defining the boundary conditions and mesh structure, simulations were conducted to investigate temperature increases in distilled water starting from 20°C, following 30 minutes of irradiation with these nanoparticles using 530 nm, 633 nm, and 785 nm light sources. The power density was taken as 100 mW/cm². The results were compared with experimental data to evaluate the model's accuracy.

2.5. Temperature Measurement with a Thermocouple During Laser Application

The non-toxic concentrations of synthesized natural MNP and MNP-Fe^{3+}, as determined in the previous experiment, were dissolved in distilled water and placed in an ultrasonic bath for approximately one hour to ensure homogeneous distribution. The solutions were irradiated for 30 minutes using light sources at 530 nm, 633 nm, and 785 nm, each adjusted to a power density of 100 mW/cm². The temperature of the solution was measured every 2.5 minutes using a thermometer (Voltcraft DT-300). The same laser irradiation procedure was applied to distilled water without nanoparticles as a control.

2.6. Photothermal Therapy Experiments

Although previous results showed that 530 nm and 633 nm light generated more heat in combination with natural MNPs, 785 nm light was chosen for the PTT experiments due to its superior tissue penetration, as reported in the literature (Stolik et al., 2000; Clement et al., 2005). The 785 nm light source available in our laboratory (CNI Laser MDL-III-785) was set to a power density of 350 mW/cm², and irradiation was applied for two durations: 10 and 20 minutes. In every plate, there were only nanoparticles and only light groups to consistently show that the potential PTT effect originated from the combination of the NP and light instead of the cytotoxicity of a high dose of nanoparticle or light. During irradiation, the plates were placed on a hot plate set to 37°C. The results of the experiments were analyzed using the MTT assay to determine which application resulted in more effective cell death.

2.7. Effect of Laser Irradiation on MRI Contrast of MNP-Fe^{3+}s

To observe the effect of light irradiation on the MRI visibility of MNPs-Fe^{3+} ion solution, we used a 7.0 T MR animal scanner (MR Solutions, MRS*DRYMAGMR) with T1-weighted sequences to image a custom-made phantom. The phantom contained laser-irradiated (785 nm, 350 mW/cm², 20 minutes) and non-irradiated MNP-Fe^{3+} ion solutions (200 µg/mL), as well as a saline control (NaCl 0.9%). A fast spin echo sequence was performed for axial imaging of solutions with a 1 mm slice thickness and matrix size of 256×256, while TR: 250, 300, 350, 400, 500, 600 ms, TE: 11 ms, and flip angle: 90°. To quantify and compare the contrast-to-noise ratio (CNR) of solutions, the acquired MR images were analyzed via a DICOM Viewer (MicroDicom Ltd., Sofia, BG).

2.8. Statistical Analysis

Figures and analyses were realized using GraphPad Prism Version 10.4.1. To analyze the difference between experimental groups in cytotoxicity and PTT results, ANOVA was followed by Tukey's multiple comparison test.

3. RESULTS

3.1. Cytotoxicity Experiments

The cytotoxicity assessed by MTT assay was significant compared to the control group for MNP and MNP-Fe^{3+} after 200 µg/mL concentration, as shown in Figure 2a and b. However, the MNP-Mn^{2+}s decreased the survival significantly after 25 µg/mL (Figure 2c), and accordingly, MNP-Mn^{2+}s was removed from the study.

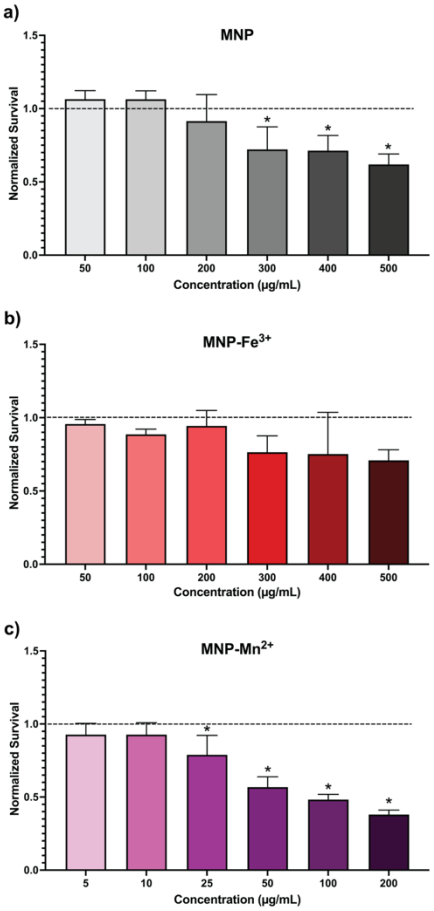

Figure 2. Cell viability of PC-3 cells was determined by MTT assay following a 24-hour incubation with (a) MNPs, (b) MNP-Fe^{3+}, and (c) MNP-Mn^{2+} at various concentrations. The data was normalized to the no-treatment control, indicated by dashed lines. Statistically significant differences ($p < 0.05$) compared to the no-treatment control are indicated by an asterisk (*).

3.2. Characterization of the Nanoparticles

The extracted MNPs and their manganese-chelated and iron-chelated counterparts were subjected to repeated washing and centrifugation steps. The resulting pellets were analyzed by scanning electron microscopy (SEM) to investigate their size distribution and morphological characteristics. As shown in Figure 3, the nanoparticles exhibited predominantly spherical shapes with rough surface textures. Due to van der Waals interactions at the nanoscale, a tendency for particle aggregation was observed. Size distribution analysis was performed using the ImageJ software by evaluating multiple SEM images (Figure 3). Based on random measurements, the average particle diameters of the MNPs and Fe-chelated MNPs were determined to be 179.3 ± 40 nm (n=100) and 152.4 ± 42 nm (n=720). To assess the hydrodynamic behavior of nanoparticles, DLS analysis was carried out. The hydrodynamic diameters of the MNPs and MNP-Fe^{3+} were found to be 206 ± 3 nm (n=3) and 214 ± 1.8 nm, respectively. The polydispersity index (PDI) values were 0.032 ± 0.019 for MNPs and 0.036 ± 0.029 for MNP-Fe^{3+}, indicating monodisperse particle distributions for both formulations, according to data (Table S1, Supporting Information). Fe-chelation did not significantly alter the particle size or hydrodynamic behavior of the nanoparticles.

The deconvolution of the C 1s spectra for MNP-Fe^{3+} revealed three distinct peaks at 284.7 eV, 286.0 eV, and 287.8 eV. The peak at 284.7 eV corresponds to C–C bonds, while the signal at 286.0 eV is attributed to C–O–C and C–OH functionalities. The peak observed at 287.8 eV indicates the presence of carbonyl groups (C=O) (Figure 4a). The N 1s spectra displayed a well-defined peak at approximately 399.7 eV, corresponding to nitrogen atoms in amine or indole-type environments, which are characteristic of the eumelanin backbone (Figure 4b). The O 1s spectra showed two distinct peaks at 531.1 eV and 532.2 eV, associated with C=O and C–O bonds, respectively, confirming the presence of carbonyl and hydroxyl functionalities within the polymeric matrix (Figure 4c). The successful coordination of Fe^{3+} ions was confirmed by the appearance of Fe 3p peaks in the XPS spectra of MNP-Fe^{3+} (Figure 4d). Although the intensity of this metal-specific peak was relatively low, semiquantitative analysis of the XPS survey

spectra revealed an atomic concentration of 0.16% for Fe. This low signal intensity can be attributed to the limited amount of metal ions introduced during the chelation process, in which the metal-to-melanin ratios were 0.1:1 for Fe. Despite their low abundance, the presence of these peaks confirms the successful incorporation of Fe^{3+} into the melanin nanoparticle matrix. Importantly, no significant shifts in binding energy or changes in peak intensity were observed in the C 1s, N 1s, or O 1s spectra between the two formulations. These findings indicate that metal ion chelation does not substantially alter the local chemical environments of carbon, nitrogen, or oxygen atoms, thereby preserving the structural integrity of the melanin core. Accordingly, the detection of characteristic C–C, C–OH, C=O, and C–N signals in the XPS spectra is consistent with the intrinsic chemical structure of melanin and confirms the successful surface characterization of the synthesized nanoparticles.

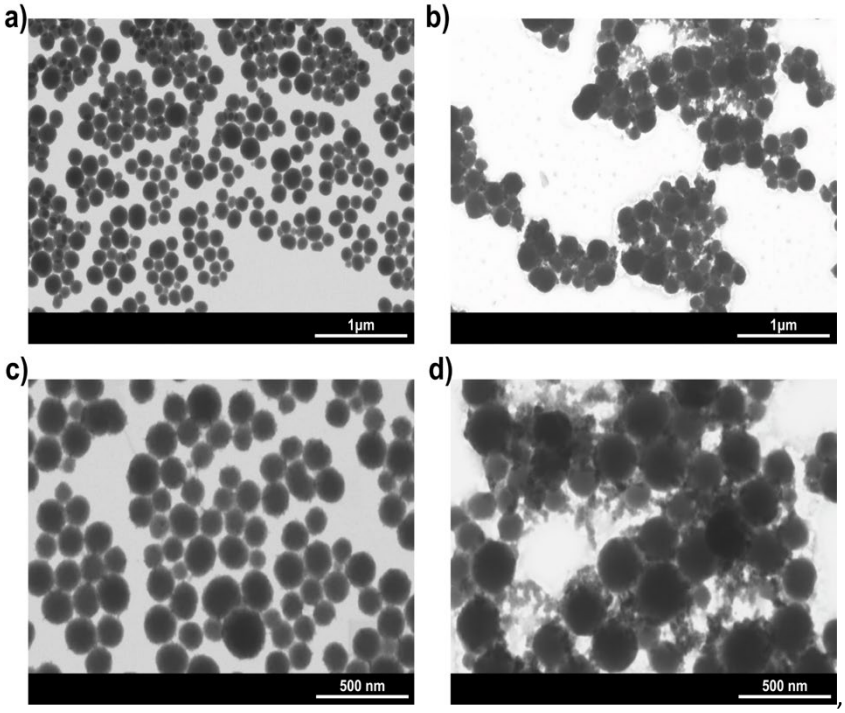

Figure 3. SEM images of MNPs (a, b) and Fe^{3+}-chelated MNPs (c, d).

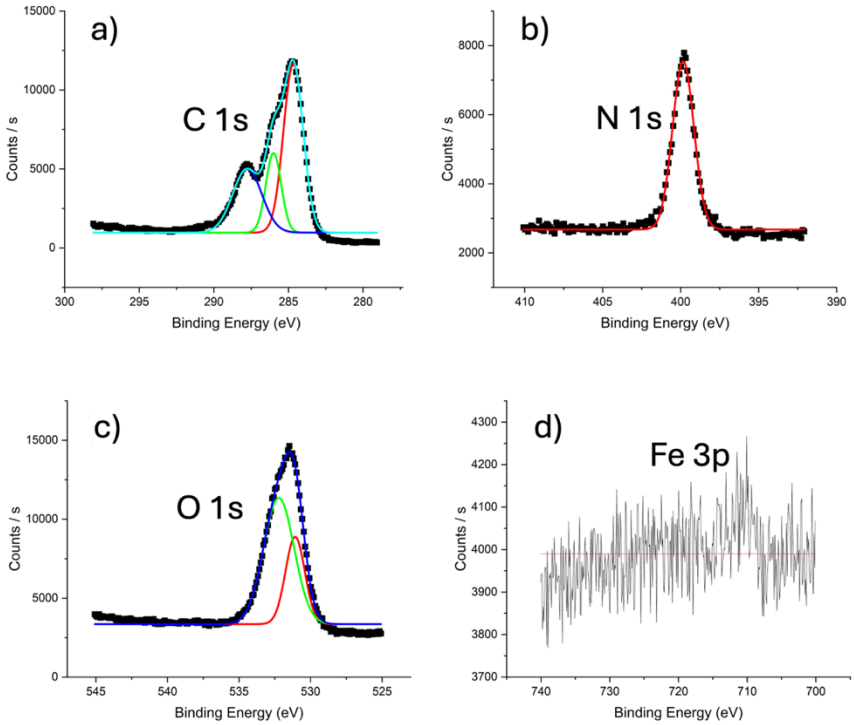

Figure 4. High-resolution XPS spectra of MNP-Fe^{3+} corresponding to C 1s, N 1s, O 1s, and Fe 3p regions.

FTIR analysis was performed on both MNP and MNP-Fe^{3+} to investigate potential structural changes following metal

ion chelation. The resulting spectra exhibited highly similar profiles for both formulations, with characteristic absorption bands associated with eumelanin's indolic and pyrrolic substructures. A broad band around 3303 cm^{-1} was attributed to O–H and N–H stretching vibrations, while additional peaks at 2926 cm^{-1} (aliphatic C–H stretching), 1550 cm^{-1} (aromatic C–N stretching), and 1329 cm^{-1} (pyrrole ring deformation) were consistently observed. Notably, no distinct peaks corresponding to Fe–O or Fe–N bonds were detected in the MNP-Fe^{3+} spectrum. This absence is likely due to the broad and intense absorption features of melanin, which can obscure subtle signals associated with low concentrations of coordinated metal ions. The complete FTIR spectrum for both samples is presented in Supporting Information, Figure S1.

3.3. Simulated Absorbance Response of Melanin NPs to Size and Iron Chelation

The results of the simulation show that the light absorption property of both MNPs and MNP-Fe^{3+}s increases with nanoparticle size and iron chelation (Figure 5).

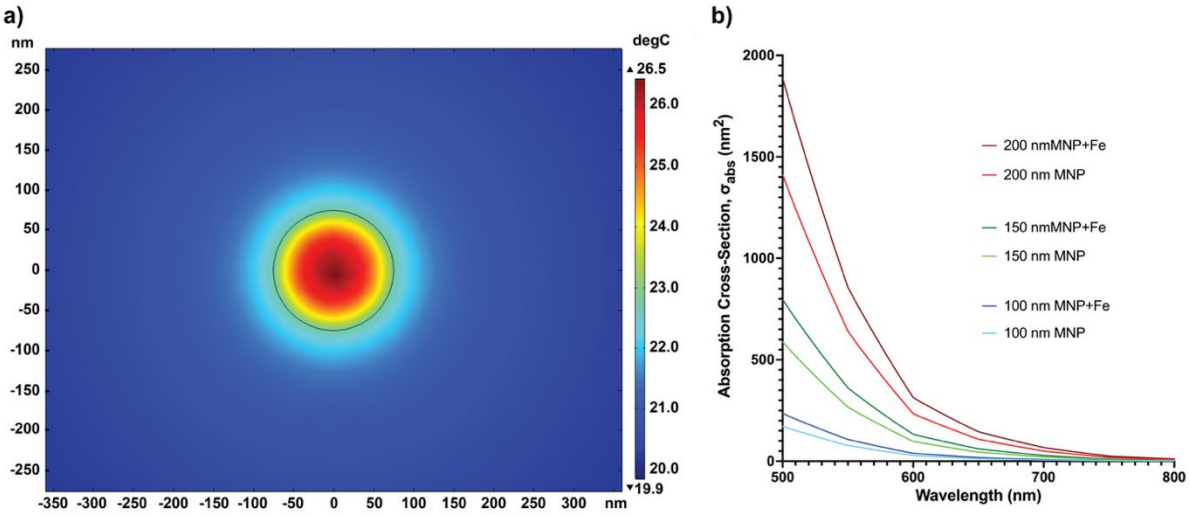

Figure 5. a) An example diagram from COMSOL that shows the simulation of an MNP during laser irradiation. b) Absorption cross-sections of MNPs (lighter colors) and MNP-Fe^{3+} (darker colors) with diameters of 100 nm (blue), 150 nm (green), and 200 nm (red), shown between 500 and 800 nm.

Table 1. Simulation results of 30 minutes of nanoparticle irradiation in distilled water, starting at an initial temperature of 20 °C

Wavelength (nm)	100 nm (MNP)	150 nm (MNP)	200 nm (MNP)	100 nm (MNP-Fe^{3+})	150 nm (MNP-Fe^{3+})	200 nm (MNP-Fe^{3+})
530	22.8°C	26.5°C	31.5°C	23.4°C	27.8°C	33.9°C
633	22°C	24.8°C	28.5°C	22.5°C	25.9°C	30.5°C
785	22°C	24.6°C	28.2°C	22.2°C	25.1°C	29°C

3.4. Temperature Measurement with a Thermocouple During Laser Application

Experimental results correlate with the simulations, revealing that 530 nm light caused the highest temperature increase, and MNP-Fe^{3+} groups reached higher temperatures than MNPs at the end of the irradiation for all light sources (Figure 6).

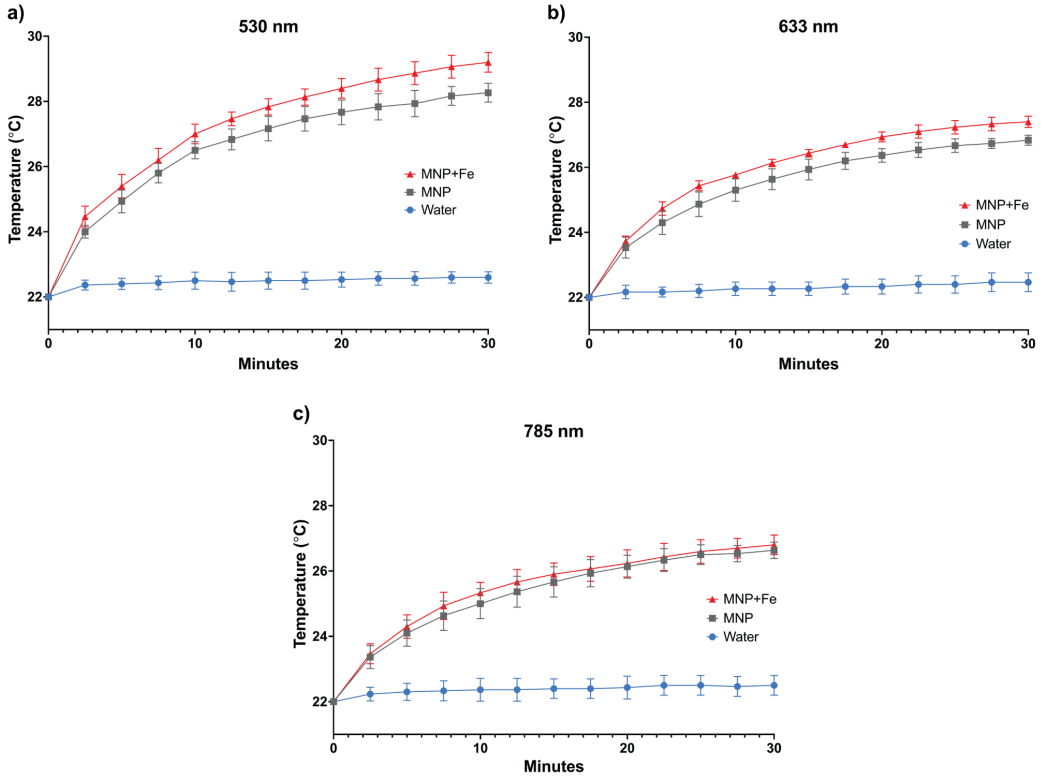

Figure 6. Experimental results of 30 minutes of MNP (gray color) and MNP-Fe^{3+} (red color) suspensions irradiation in distilled water using a) 530 nm, b) 633 nm, and c) 785 nm light sources. Irradiation of water without nanoparticles was shown as blue data points.

3.5. Photothermal Therapy Experiments (785 nm)

As shown in Figure 7, PTT applied to PC-3 cells for 10 and 20 minutes resulted in a significant decrease in cell survival compared to the control groups, with the most pronounced effect (approximately a 75% reduction) observed in the group treated with MNP-Fe^{3+}-mediated PTT for 20 minutes.

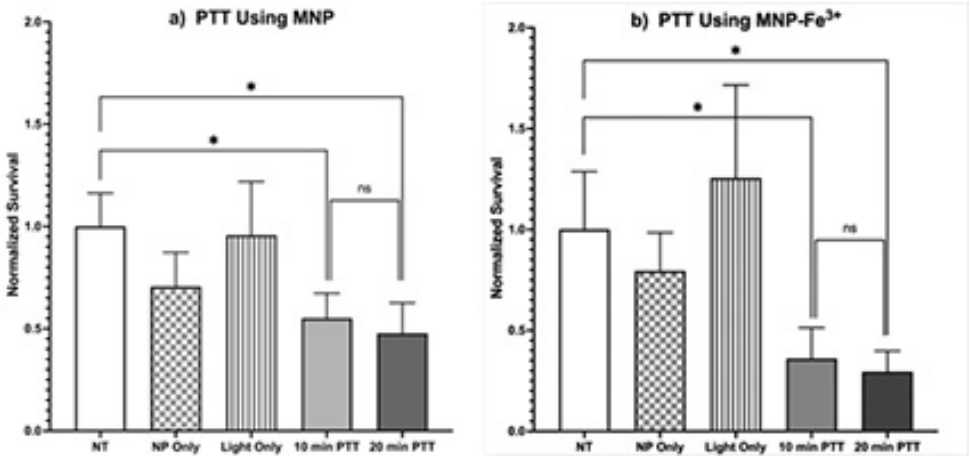

Figure 7. PTT results using a) 200 µg/mL MNPs and b) 200 µg/mL MNPs-Fe^{3+}. A 785 nm light source with an energy density of 350 mW/cm² was used in the "Light Only" PTT groups. Statistically significant differences ($p < 0.05$) compared to the no-treatment control are indicated by an asterisk (*). ns stands for "Not significant".

3.6. Effect of Laser Irradiation on MRI Contrast of MNP-Fe^{3+}s

Image analysis using the DICOM viewer revealed that laser-irradiated and non-irradiated MNP-Fe^{3+} solutions at 200 µg/mL concentration presented higher CNR compared to the control (saline water) in a 7.0 T animal MRI scanner, with mean values of 1046.15 ± 70.75, 971.08 ± 76.95, and 896.67 ± 75.19, respectively (Figure 8). Consistent with the T1 shortening effect of MNP-Fe^{3+} ion solutions that are presented in our previous studies, MNP-Fe^{3+} solutions provided better CNR intensities compared to the saline water (Baysoy et al., 2023; Baysoy et al., 2023; Bayrak et al., 2025). There is a slight decrease in CNR values of the

MNP-Fe^{3+} ion solution after laser exposure compared to the non-exposed MNP-Fe^{3+} ion solution at all slices obtained with varied TR values, including 250, 300, 350, 400, 500, and 600 (Figure S2, Supporting Information).

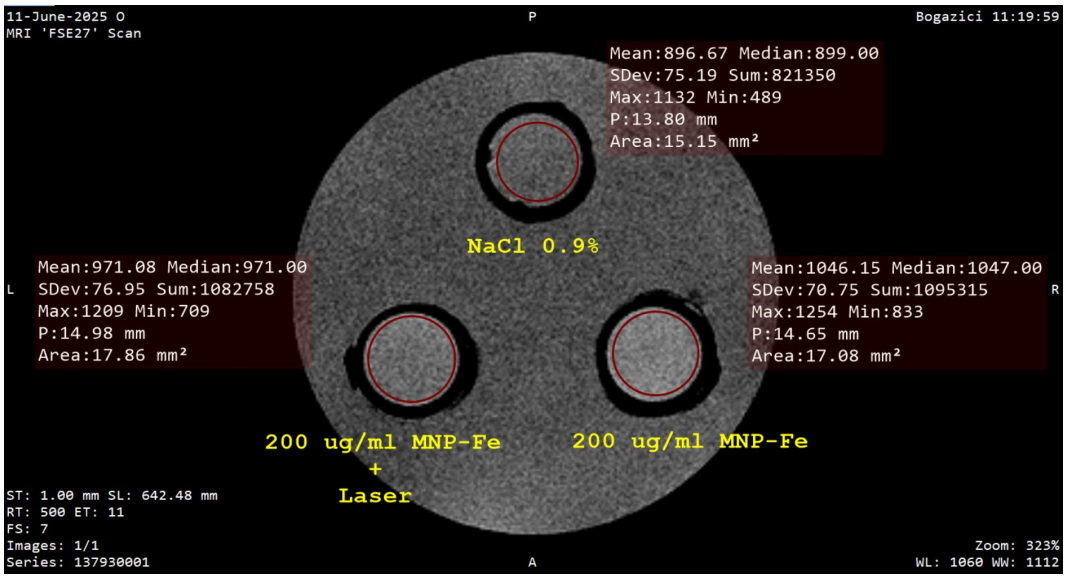

Figure 8. CNR measurements of the saline water (indicated in yellow font as NaCl 0.9%) and MNP-Fe^{3+} ion solutions at 200 µg/mL concentration before (indicated in yellow font as 200 µg/mL MNP-Fe) and after laser irradiation (indicated in yellow font as 200 µg/mL MNP-Fe^{3+} Laser) using DICOM Viewer.

4. DISCUSSION

There are studies in which MNPs chelated with metal ions were used simultaneously for imaging and therapy, i.e., for theranostic purposes. However, the influence of metal ion chelation on the PTT performance of MNPs and the effects of PTT application on MR contrast remain insufficiently understood. This study aims to investigate these effects through both silico modeling and experimental approaches.

In the initial stage of the experiments, nanoparticles-chelated with both manganese and iron were produced; however, manganese-bound MNPs, which were found to be cytotoxic at 50 µg/mL ($p = 0.016$) and higher concentrations, were excluded from the subsequent experiments. Results also confirmed that MNP-Fe^{3+}s were not significantly cytotoxic at any concentration tested. In contrast, concentrations of the MNPs higher than 200 µg/mL were significantly cytotoxic compared to the no-treatment control (see Figure 2). The characterization of both MNPs and Fe-chelated MNPs exhibited spherical morphology with rough surfaces and monodisperse size distributions. SEM and DLS analyses confirmed average particle sizes of approximately 179 nm and 152 nm, respectively, along with hydrodynamic diameters of 228 nm and 214 nm. Fe-chelation did not significantly affect particle size or colloidal stability. XPS analysis confirmed the successful incorporation of Fe^{3+} ions without altering the local chemical environments of carbon, nitrogen, or oxygen within the melanin structure. Simulation results presented in Figure 5b suggested that nanoparticle size is directly proportional to light absorption and that iron-chelated nanoparticles absorb light more effectively than non-chelated ones. In line with this finding, experiments showed that MNP-Fe^{3+} increased the solution temperature more than unchelated MNPs during irradiation. Additionally, the experimentally observed temperature increases after 30 minutes of irradiation were comparable to the simulation results, indicating that the computational model accurately simulates the heat generation property of the nanoparticles. For example, the temperature increase suggested by the simulation for 150 nm nanoparticles after irradiation at 785 nm was 4.6°C for MNP and 5.1°C for MNP-Fe^{3+}. The experimental results for the same conditions were 4.6°C (MNP) and 4.8°C (MNP-Fe^{3+}). Subsequent experiments demonstrated that both types of synthesized nanoparticles induced cell death through PTT, and, consistent with previous results, iron-chelated melanin was found to have superior PTT efficacy. However, for both nanoparticles, the duration of light irradiation did not significantly affect the survival of cells. In summary, all results indicate that chelation with iron does not reduce the PTT efficacy of MNPs; rather, it may enhance it. This enhancement may be due to increased light absorption resulting from the formation of metal–melanin complexes, which can alter the electronic structure of melanin and improve its photothermal conversion efficiency. Previous studies have shown that chelation of metal ions, such as Fe^{3+}, can lead to changes in the optical properties of melanin by narrowing the bandgap, thereby enhancing heat generation upon irradiation (Zou et al., 2020; Mavridi-Printezi et al., 2023).

Finally, the change in contrast of MNP-Fe^{3+}s after PTT was examined, and a consistent decrease in CNR in the irradiated group was observed for all acquired T1-weighted

images with various TR values. The presence of a high amount of O and OH groups in the MNPs' chemical structure, as well as the production of singlet oxygen (O reduction) under light irradiation, has been previously reported (Umur et al., 2024; Obukhova et al., 2025). Probably, the O_2 reduction after light irradiation affects the H binding capability of MNPs-Fe nanoparticles in the surrounding water, leading to an increase in T1 relaxivity rates and a slight reduction in CNR. Although further evaluation is necessary, these results suggest that MNP-Fe^{3+} nanoparticles remain detectable by MRI during PTT and that the measurable decrease in their contrast may be used for PTT dosimetry.

One of the major limitations of this study is the absence of *in vivo* experiments; thus, factors such as circulation, immune system interactions, and light attenuation are not reflected in the results. A second limitation is that the simulations were conducted using a single nanoparticle. Future studies will focus on utilizing MNP-Fe^{3+} in *in vivo* experiments, integrating drug delivery methods, and enhancing simulations to incorporate multiple nanoparticles.

4. CONCLUSIONS

Results showed that while ferric ion-chelation does not increase cytotoxicity, manganese chelation significantly decreases the survival rate of PC-3 cells. Both computational modeling and experimental results indicate that chelation with ferric ions increases the photothermal efficacy of the MNPs. PTT applied to PC-3 cells for 10 and 20 minutes resulted in a significant reduction in cell viability compared to control groups, with the greatest reduction, more than 70%, observed in the 20-minute MNP-Fe^{3+}-mediated PTT group. Finally, the MRI experiment results revealed that the MRI contrast of MNP-Fe^{3+}s decreased slightly after irradiation with light.

This research aimed to investigate the PTT and MRI performance of metal ion-chelated natural melanin MNPs, and the results suggest that MNP-Fe^{3+} causes less significant toxicity and higher PTT efficacy than MNPs. Furthermore, the MRI contrast of MNP-Fe^{3+}s decreases after laser irradiation, which suggests that these nanoparticles can be used for real-time monitoring of PTT in theranostic applications. Future studies should focus on testing MNP-Fe^{3+} using improved computational and experimental models, such as simulating the interactions of multiple nanoparticles and performing an MRI-guided PTT on animal disease models.

Author Contributions

Melike DEMİRTAŞ: (c) Literature Review, (f) Data Collection, (g) Data Analysis, Interpretation, (h) Drafting Article

Şeyma YEKTAR: (c) Literature Review, (f) Data Collection, (g) Data Analysis, Interpretation, (h) Drafting Article

Gizem KALELİ CAN: (c) Literature Review, (e) Material, Resource Supply, (f) Data Collection, (g) Data Analysis, Interpretation, (h) Drafting Article

Alpay ÖZCAN: (e) Material, Resource Supply, (f) Data Collection, (ı) Critical Review

Engin BAYSOY: (a) Original Idea, (b) Study Design, Methodology, (c) Literature Review, (d) Supervision, (e) Material, Resource Supply, (f) Data Collection, (g) Data Analysis, Interpretation, (h) Drafting Article

Mustafa Kemal RUHİ: (a) Original Idea, (b) Study Design, Methodology, (c) Literature Review, (d) Supervision, (e) Material, Resource Supply, (f) Data Collection, (g) Data Analysis, Interpretation, (h) Drafting Article

Declaration of Ethical Code

I n this study, we affirm that all the necessary rules under the "Regulation on Scientific Research and Publication Ethics in Higher Education Institutions" have been adhered to, and none of the actions mentioned under the title "Actions Contrary to Scientific Research and Publication Ethics" in the mentioned regulation have been conducted.

Conflict of Interest

The authors declare no conflict of interest.

REFERENCES

Bayrak, E., Bayır, E., Baysoy, E., Özcan, A., Ayan, B., Saygılı, E., & Kaleli-Can, G. (2025). Nintedanib loaded iron (III) chelated melanin nanoparticles as an MRI-visible antifibrotic drug delivery system. *Colloids and Surfaces B: Biointerfaces, 252*, 114652. https://doi.org/10.1016/j.colsurfb.2025.114652

Baysoy, E., Ayan, B., Kaleli-Can, G., & Büyüksaraç, B. (2023, November 10-12). *Passive device tracking for interventional MRI with ferric ion chelated natural melanin nanoparticles* [Paper presentation]. 2023 Medical Technologies Congress (TIPTEKNO), Famagusta, Cyprus. IEEE.

Baysoy, E., Kaleli-Can, G., Ayan, B., Özcan, A., Kocatürk, Ö., & Liu, C. (2024). Kiosk 10R-TC-09 – Enhanced balloon catheter visualization with biocompatible melanin nanoparticles in 3T MRI. *Journal of Cardiovascular Magnetic Resonance, 26*, 100278. https://doi.org/10.1016/j.jocmr.2024.100278

Baysoy, E., Kaleli Can, G., Özcan, A., & Liu, C. (2023). Passive device tracking for interventional MRI with

ferric ion chelated natural melanin nanoparticles. *ISMRM 2023 - Proceedings of the International Society for Magnetic Resonance in Medicine, 31*. [Abstract]

Caldas, M., Santos, A. C., Veiga, F., Rebelo, R., Reis, R. L., & Correlo, V. M. (2020). Melanin nanoparticles as a promising tool for biomedical applications: A review. *Acta Biomaterialia, 105*, 142–157. https://doi.org/10.1016/j.actbio.2020.01.044

Chen, A., Sun, J., Liu, S., Li, L., Peng, X., Ma, L., & Zhang, R. (2020). The effect of metal ions on endogenous melanin nanoparticles used as magnetic resonance imaging contrast agents. *Biomaterials Science, 8*(1), 379–390. https://doi.org/10.1039/c9bm01580a

Clement, M., Daniel, G., & Trelles, M. (2005). Optimising the design of a broad-band light source for the treatment of skin. *Journal of Cosmetic and Laser Therapy, 7*(3-4), 177–189. https://doi.org/10.1080/14764170500344575

Cordero, R. J. B., & Casadevall, A. (2020). Melanin. *Current Biology, 30*(4), R142–R143. https://doi.org/10.1016/j.cub.2019.12.042

Dong, Z., Gong, H., Gao, M., Zhu, W., Sun, X., Feng, L., Fu, T., Li, Y., & Liu, Z. (2016). Polydopamine nanoparticles as a versatile molecular loading platform to enable imaging-guided cancer combination therapy. *Theranostics, 6*(7), 1031–1042. https://doi.org/10.7150/thno.14431

Eom, T., Woo, K., Cho, W., Heo, J. E., Jang, D., Shin, J. I., Martin, D. C., Wie, J. J., & Shim, B. S. (2017). Nanoarchitecturing of natural melanin nanospheres by layer-by-layer assembly: Macroscale anti-inflammatory conductive coatings with optoelectronic tunability. *Biomacromolecules, 18*(6), 1908–1917. https://doi.org/10.1021/acs.biomac.7b00336

Ju, K. Y., Lee, J. W., Im, G. H., Lee, S., Pyo, J., Park, S. B., Lee, J. H., & Lee, J. K. (2013). Bio-inspired, melanin-like nanoparticles as a highly efficient contrast agent for T1-weighted magnetic resonance imaging. *Biomacromolecules, 14*(10), 3491–3497. https://doi.org/10.1021/bm4008138

Kang, S., Baskaran, R., Ozlu, B., Davaa, E., Kim, J. J., Shim, B. S., & Yang, S. G. (2020). T(1)-Positive Mn(2+)-Doped multi-stimuli responsive poly(L-DOPA) nanoparticles for photothermal and photodynamic combination cancer therapy. *Biomedicines, 8*(10), 417. https://doi.org/10.3390/biomedicines8100417

Liu, Y., & Simon, J. D. (2003). The effect of preparation procedures on the morphology of melanin from the ink sac of Sepia officinalis. *Pigment Cell Research, 16*(1), 72–80. https://doi.org/10.1034/j.1600-0749.2003.00009.x

Mavridi-Printezi, A., Menichetti, A., Mordini, D., & Montalti, M. (2023). Functionalization of and through melanin: Strategies and bio-applications. *International Journal of Molecular Sciences, 24*(11), 9689. https://doi.org/10.3390/ijms24119689

Miao, Z. H., Wang, H., Yang, H., Li, Z. L., Zhen, L., & Xu, C. Y. (2015). Intrinsically Mn2+-chelated polydopamine nanoparticles for simultaneous magnetic resonance imaging and photothermal ablation of cancer cells. *ACS Applied Materials & Interfaces, 7*(31), 16946–16952. https://doi.org/10.1021/acsami.5b06265

Obukhova, T., Semenenko, M., Dusheiko, M., Davidenko, S., Davidenko, Y. S., Davidenko, S. S., Malyuta, S., Shahan, S., Pylypchuk, O. S., Mochuk, P., Voitovych, M., Kuzmenko, T., & Sarikov, A. (2025). Optical studies of melanin films as a material for solar light absorbers. *Materials Research Express, 12*(2), 025401. https://doi.org/10.1088/2053-1591/ade227

Solano, F. (2017). Melanin and melanin-related polymers as materials with biomedical and biotechnological applications—Cuttlefish ink and mussel foot proteins as inspired biomolecules. *International Journal of Molecular Sciences, 18*(7), 1561. https://doi.org/10.3390/ijms18071561

Stolik, S., Delgado, J. A., Perez, A., & Anasagasti, L. (2000). Measurement of the penetration depths of red and near infrared light in human "ex vivo" tissues. *Journal of Photochemistry and Photobiology B: Biology, 57*(2-3), 90–93. https://doi.org/10.1016/s1011-1344(00)00082-8

Sun, J., Xu, W., Li, L., Fan, B., Peng, X., Qu, B., Wang, L., Li, T., Li, S., & Zhang, R. (2018). Ultrasmall endogenous biopolymer nanoparticles for magnetic resonance/photoacoustic dual-modal imaging-guided photothermal therapy. *Nanoscale, 10*(22), 10584–10595. https://doi.org/10.1039/c8nr01215f

Umur, E., Arslan, F., Bakay, E., Sirek, B., Ayan, B., Baysoy, E., Topaloğlu, N., & Kaleli-Can, G. (2024). Layer-by-layer assembled melanin nanoparticles thin films for photodynamic activity-based disinfection by ultraviolet A irradiation. *Emergent Materials, 7*, 1259–1270. https://doi.org/10.1007/s42247-024-00761-7

Xu, W., Sun, J., Li, L., Peng, X., Zhang, R., & Wang, B. (2017). Melanin-manganese nanoparticles with ultrahigh efficient clearance in vivo for tumor-targeting T1 magnetic resonance imaging contrast agent. *Biomaterials Science, 6*(1), 146–155. https://doi.org/10.1039/c7bm00635g

Zou, Y., Wu, T., Li, N., Guo, X., & Li, Y. (2020). Photothermal-enhanced synthetic melanin inks for near-infrared imaging. *Polymer, 186*, 122042. https://doi.org/10.1016/j.polymer.2019.122042